Fast scanned widefield scheme provides tunable and uniform illumination for optimized SMLM on large fields of view

Adrien Mau[1,2]*, Karoline Friedl[2,3], Christophe Leterrier[3], Nicolas Bourg[2] & Sandrine Lévêque-Fort[1]*

1 Université Paris-Saclay, CNRS, Institut des Sciences Moléculaires d'Orsay, 91405, Orsay, France.
2 Abbelight, 191 avenue Aristide Briand, Cachan, France.
3 Aix-Marseille Université, CNRS, INP UMR7051, NeuroCyto, Marseille, France.
* Corresponding authors : adrien.mau@u-psud.fr , sandrine.leveque-fort@u-psud.fr

Abstract

Quantitative analyses in classical fluorescence microscopy and Single Molecule Localization Microscopy (SMLM) require uniform illumination over the field of view; ideally coupled with optical sectioning techniques such as Total Internal Reflection Fluorescence (TIRF) to remove out of focus background. In SMLM, high irradiances (several kW/cm²) are crucial to drive the densely labeled sample into the single molecule regime, and conventional gaussian-shaped lasers will typically restrain the usable field of view to around 40 µm x 40 µm. Here we present Adaptable Scanning for Tunable Excitation Regions (ASTER), a novel and versatile illumination technique that generates uniform illumination over adaptable fields of view and is compatible with illumination schemes from epifluorescence to speckle-free TIRF. For SMLM, ASTER delivers homogeneous blinking kinetics at reasonable laser power, providing constant precision and higher throughput over fields of view 25 times larger than typical (up to 200 µm x 200 µm). This allows improved clustering analysis and uniform size measurements on sub-100 nm objects, as we demonstrate by imaging nanorulers, microtubules and clathrin-coated pits in COS cells, as well as periodic β2-spectrin along the axons of neurons. ASTER's sharp, quantitative TIRF and SMLM images up to 200 µm x 200 µm in size pave the way for high-throughput quantification of cellular structures and processes.

Introduction

In advanced widefield fluorescence microscopy, lasers are a common excitation source: they provide excitation at precise wavelengths and possess high spatial coherence, both properties that are crucial to obtain quantifiable images. Typically, the laser is focused at the Back Focal Plane (BFP) of the objective to produce a large collimated beam illuminating the whole sample. While widefield fluorescence microscopy is a fast imaging method, resulting images are usually contaminated by blur from below and above the plane of focus, clouding the fluorescence signal.

Optical sectioning improves the signal by spatially limiting the illumination around the focal plane: Highly Inclined and Laminated Optical Sheet (HiLo) excitation translates the laser beam in the BFP to an oblique illumination of the sample[1]. Placing the beam at the position corresponding to illumination at the critical angle results in a "grazing incidence", ~1-µm thick illumination sheet above the coverslip[2,3]. Inclining the beam further[4] results in Total Internal Reflection Fluorescence (TIRF[5]), restraining the illumination to an exponentially decreasing intensity over a few tens of nanometers above the coverslip surface. These remarkable sectioning capabilities can be performed on one single setup[6–8] and allow to study membrane and adhesion processes with minimal background. In practice, however, TIRF suffers from heterogeneous illumination caused by the interference patterns arising from the high spatial coherence of lasers and scattering. Rapidly spinning the beam around the BFP can alleviate these fringes by averaging beam orientations over a single camera frame[9], a method since applied with several variants and refinements[10–12].

The methods above result in Gaussian-shaped illumination profiles over the sample. This is sufficient for the typical Field of View (FOV) acquired by EMCCD cameras but is more problematic over larger FOVs acquired by newer, highly-sensitive sCMOS cameras[13]. The non-uniformity of Gaussian-shaped illumination lowers exploitable FOV sizes and thereby decreases the imaging throughput, a significant caveat for quantitative analysis of images obtained by TIRF.

The need for uniform excitation is even more pressing in Single Molecule Localization Microscopy (SMLM). The key condition for SMLM is the obtention of a single molecule regime (<<1 emitting molecule/1 µm^3) from densely labeled samples, and this relies on driving most fluorophores in a dark state. Whether in (f)PALM[14,15], (d)STORM[16–18] or PAINT[19] (SMLM strategies), the single molecule regime is reached by high irradiance with the excitation source (kW/cm^2). As the transition to the dark state is highly dependent on the local excitation intensity, non-uniformities of illumination result in a strongly heterogeneous blinking behavior and loss of image quality across

the FOV. This additional constraint precludes proper analysis of SMLM images over large fields of view.

Thus, several recent studies have aimed at obtaining a uniform excitation over a large FOV. Classical solutions revolve around beam-reshapers[20–23], multimode fibers[24–26] and Spatial light modulators (piSMLM[27]). These methods illuminate the whole field at once, so provide larger FOVs under the premise of using higher laser power. However, focusing a high-power laser beam at the edge of the BFP can damage the lens at the back of the objective. piSMLM can adapt the shape and size of the FOV, but causes high power loss, and its ability to perform in TIRF has not been demonstrated so far. Waveguides[28–30], on the other hand, provide excellent fixed TIRF on extremely large fields, but cannot be restricted to the actual FOV acquired by the camera, illuminating and bleaching the whole sample at once.

To circumvent the compromise between laser power requirements, optical sectioning performances and field uniformity, we developed ASTER (Adaptable Scanning for Tunable Excitation Region). This illumination strategy can perform epifluorescence, oblique or TIRF illumination, while providing illumination uniformity at variable FOV sizes adapted to the camera or sample. ASTER is a general widefield illumination scheme that can provide benefits to both classical widefield fluorescence microscopy and SMLM.

Flat-Top Epifluorescence/TIRF excitation

ASTER is a hybrid scanning and widefield excitation scheme. The initial base Gaussian beam, which provides a limited and non-uniform excitation, is combined with a scanning unit to generate a large, uniform illumination. In practice we used two galvanometer scanning mirrors placed in a plane conjugated to the BFP of the objective. The Gaussian-shaped excitation beam is focused in between the mirrors (Fig. 1a) so that an angle shift applied to the mirrors will induce a similar angle shift in the objective BFP and a position shift of the beam at sample plane, allowing for large XY area scans. Moving the Gaussian beam position in defined patterns such as raster scan or an Archimedes spiral generates an overall homogeneous illumination (Supplementary Fig. 1) over the FOV when averaged over the camera frame exposure time. Notably, as the polar angle of the beam varies at the BFP while its position is maintained, this flat-top excitation scheme allows for inclined illumination such as oblique or TIRF. A conventional motorized translation stage serves as switch from epifluorescence to oblique and TIRF excitation[31,32].

To generate a truly uniform flat-top excitation over the whole FOV, the scanning needs to meet certain criteria. First, the maximum distance between adjacent lines on the beam path has to be lower than 1.2 σ (Supplementary Fig. 1), σ being the standard deviation of the input gaussian excitation beam. This defines - for a given field size - the minimum number of lines needed to achieve homogeneity. Second, a typical galvanometer mirror has a repositioning delay of 200 µs, so the number of scanned lines will set the minimal required time to synthesize the flat top profile. Our implementation uses an input excitation beam of σ = 17 µm: ten lines are sufficient to generate a flat-top profile on the largest (220 µm x 220 µm) FOV at 500 Hz, which is 5 times the maximum frame rate of classical sCMOS (100 fps) camera. In practice, we used camera integration times between 50 to 100 ms with flat-top profiles generated at 100 – 40 Hz. A smaller base gaussian beam would result in a sharper flat-top profile, but at the cost of slower imaging speed as more lines have to be scanned. Note that - compared to confocal laser scanning - ASTER does not perform point scanning, but a continuous scan with a wide input collimated beam, and thus can cover large areas much faster.

To characterize the illumination homogeneity and validate our simulations, we imaged a thin layer of fluorescent Nile Blue with a classical wide Gaussian beam excitation (σ =

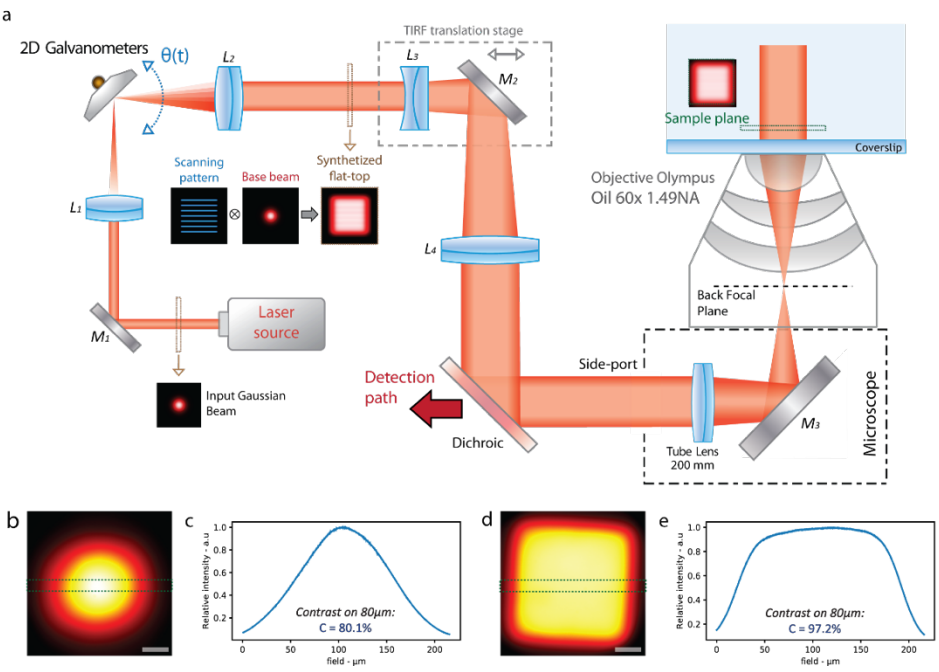

Fig. 1 Schematic of ASTER and resulting illumination patterns.
a Schematic of the ASTER setup to generate a homogeneous field using a raster scanning pattern. Li are lenses with focal length fi: f1=100, f2=100, f3=-35, f4=250. M1, M2 and M3 are mirrors. A small input Gaussian base beam is scanned in-between the L1 and L2 lenses, resulting in a collimated flat-top profile, which then goes through a TIRF translation stage and is magnified between L2 and L3. After focalization at the BFP of an objective lens, it results in a temporally averaged flat-top excitation profile at the sample. (b-e) Thin layer of fluorescent Nile-Blue imaged at low laser power with a fixed Gaussian excitation beam (b,c) and with ASTER (d,e) raster scanning excitation. Intensity graphs (c,e) are respective horizontal intensity profiles of Gaussian and ASTER illumination taken along the green dashed area. The Michelson contrast at 40 µm from the image center is also indicated. Scalebars 40 µm (b,d).

45 µm) and with our ASTER illumination scanning a raster pattern of ten 150 µm long lines (Fig. 1b-e). (Fig. 1d) shows that the ASTER illumination allows for the homogeneous excitation of Nile Blue fluorescence over a single camera frame, with a square shape matched to typical camera detectors. The resulting flat-top illumination profile is consistent with our simulations (Supplementary Fig. 1) and exhibits significant flatness over approximately 120 µm, which could be diminished or increased by adapting the scanning path. To quantify homogeneity, we measured the local Michelson contrast[33] at different distances from the center of the FOV. At a radial distance of 40 µm, the Gaussian illumination had a contrast of 80.1%, while ASTER's contrast was of 97.2%. If we consider that contrast should be superior to 95% over the whole usable FOV, the Gaussian illumination would be limited to a 30 µm x 30 µm usable FOV, while ASTER can provide at least a ~15X larger, 115 µm x 115 µm FOV.

We then assessed the compatibility of ASTER with inclined, optically-sectioning illumination schemes, where a precise alignment and focusing of the excitation beam in the BFP of the objective is crucial (Supplementary Fig. 2). We focused on TIRF, as it is one of the most common schemes used in SMLM. First, we compared TIRF to epi illumination obtained through ASTER by imaging 3-µm diameter beads, coated with biotin and labelled with AF647-streptavidin (Supplementary Fig. 3) on a 160 µm x 160 µm FOV. (Fig. 2a-b) are crops from whole images of this experiment; the beads apparent radii are dependent on the penetration depth of the illumination[34,35] and thus reflect the characteristics of each excitation scheme. As expected, the measured penetration depth for TIRF excitation is around 100 nm, while epi fluorescence yields a mean depth of 800 nm, likely defined by the objective's depth of field (Fig. 2c). The penetration depths for both schemes are uniform over the FOV, and their variations shows no spatial correlation, demonstrating the absence of a spatial excitation anisotropy. Variation between beads more likely stem from both measurement precision and physical discrepancy of the bead population.

To assess the optical sectioning efficiency in experimental conditions, we imaged rat hippocampal neurons labeled for ß2-spectrin, a submembrane scaffold protein lining the neuronal plasma membrane, and revealed with AF647. We compared epi and TIRF configurations on a 200 µm x 200 µm FOV, the whole field of our sCMOS Camera (Fig. 2d-e). The images show that ASTER with TIRF maintains the quality of optical sectioning along the whole FOV: Fluorescence over the cell bodies of neurons (parts that are thicker than the illumination depth) exhibit less blurred fluorescence, and a better signal can be observed compared to the epi-illuminated image, revealing the delicate structure of the neuronal network. A disadvantage of TIRF with classic Gaussian-shaped laser beams are interference speckles: TIRF with ASTER, by contrast, exhibits no such inhomogeneous patterns, as they are likely to be averaged out by beam scanning and camera integration. In conclusion, ASTER leads to TIRF images with a similar quality as spinning azimuthal TIRF, with the added benefit of field uniformity and FOV size versatility. ASTER illumination efficiently provides both uniform spatial illumination and uniform axial optical sectioning for fluorescence microscopy in both epi and TIRF illumination.

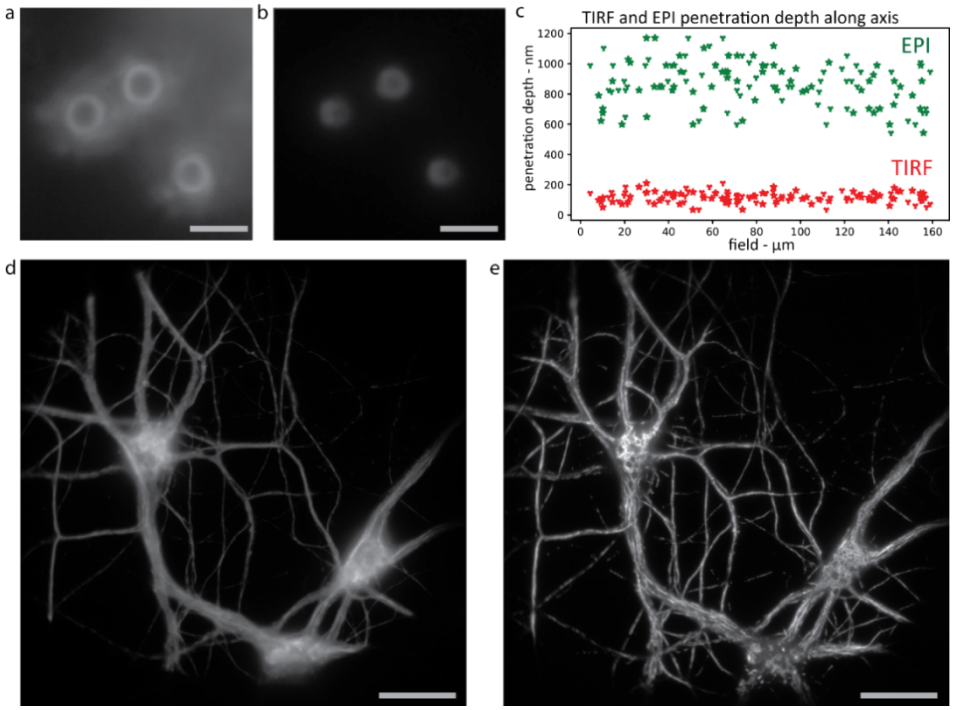

Fig. 2 ASTER TIRF Illumination. (a-c) Illumination of 3 µm beads with focus at the coverslip, in ASTER epifluorescence (a) and ASTER TIRF (b) illumination (whole images are shown in Supplementary Figure 3). Scalebars 4 µm. (c) Measured penetration depth for individual beads in EPI (green) and TIRF (red) illuminations on a large 200 µm x 200 µm FOV. Stars and Y-shaped markers respectively denote measurement along the x and y axis of the sample plane. (d-e) 200 µm x 200 µm imaging FOV of neurons labeled with an anti-β2-spectrin primary and an AF647-coupled secondary antibody, illuminated with raster-scanning ASTER, and an exposure time of 100 ms, in either epifluorescence (e) or TIRF (d) illumination scheme. Scalebars 40 µm.

Large Field Uniform SMLM Imaging

Next, we applied ASTER to SMLM experiments, namely DNA-Point Accumulation in Nanoscale Topography (PAINT) and STochastic Optical Reconstruction Microscopy (STORM). To assess the effect of ASTER illumination FOV size and homogeneity in SMLM experiments, and compare it to a classical Gaussian illumination, we first imaged three-spot, 40 nm spaced nanorulers using DNA-PAINT (Fig. 3). Three different TIRF excitation schemes (Gaussian, ASTER on a 70 µm x 70 µm FOV, and ASTER on 120 µm x 120 µm

FOV) were used, with the other parameters remaining identical. In the single molecule regime, each of the three nanoruler spot acts as a source of blinking fluorescence, resulting in a set of localizations spread by the pointing accuracy of each blinking event. For analysis we applied the following algorithm: first, individual nanorulers were isolated by DBscan clustering[36], then a Gaussian Mixture Model fit identified each of the three peaks within a single nanoruler (see Methods, Supplementary Fig. 5). The mean position and standard deviation were extracted from the peak fit of each spot. These two parameters allowed to estimate the local localization precision and resolution capability.

The gaussian excitation resulted in a bell-shaped localization precision: at the center of the FOV, the localization precision is only 7 nm, but it quickly increases with the distance to FOV center. At 20 µm it is 8 nm, and up to 11 nm at the edges of the FOV, 1.6 times worse than at center (Fig. 3d,g). Meanwhile, ASTER excitation on a similar FOV provided a uniform localization precision of 7.6 nm - even at 30 µm from the center of the FOV (Fig. 3b, g). On a large 120 µm x 120 µm FOV with similar parameters, ASTER provided a uniform 9 nm localization precision (Fig. 3c, g). This means that a 20X increase in the FOV size came at the cost of a 1.3 worse localization precision. It is conceivable that a localization precision below 9 nm could be reached by carefully optimizing imaging parameters such as laser power, optical sectioning and camera integration time. Moreover, the inhomogeneity of the Gaussian illumination strongly impacted the size estimation of the nanorulers along the FOV (Fig. 3h). We measured the end-to-end size of the identified nanorulers (ground truth value 80 nm). The relative size error from Gaussian beam illuminated images was 1% at the center of FOV, rising to 4% at 35 µm from the center. ASTER provided more homogeneous measurements: the relative size error remained at 0.5% up to 45 µm from the center of the FOV. All the illumination conditions resulted in similar mean values for the nanoruler size (Fig. 3i), but we observed an increased

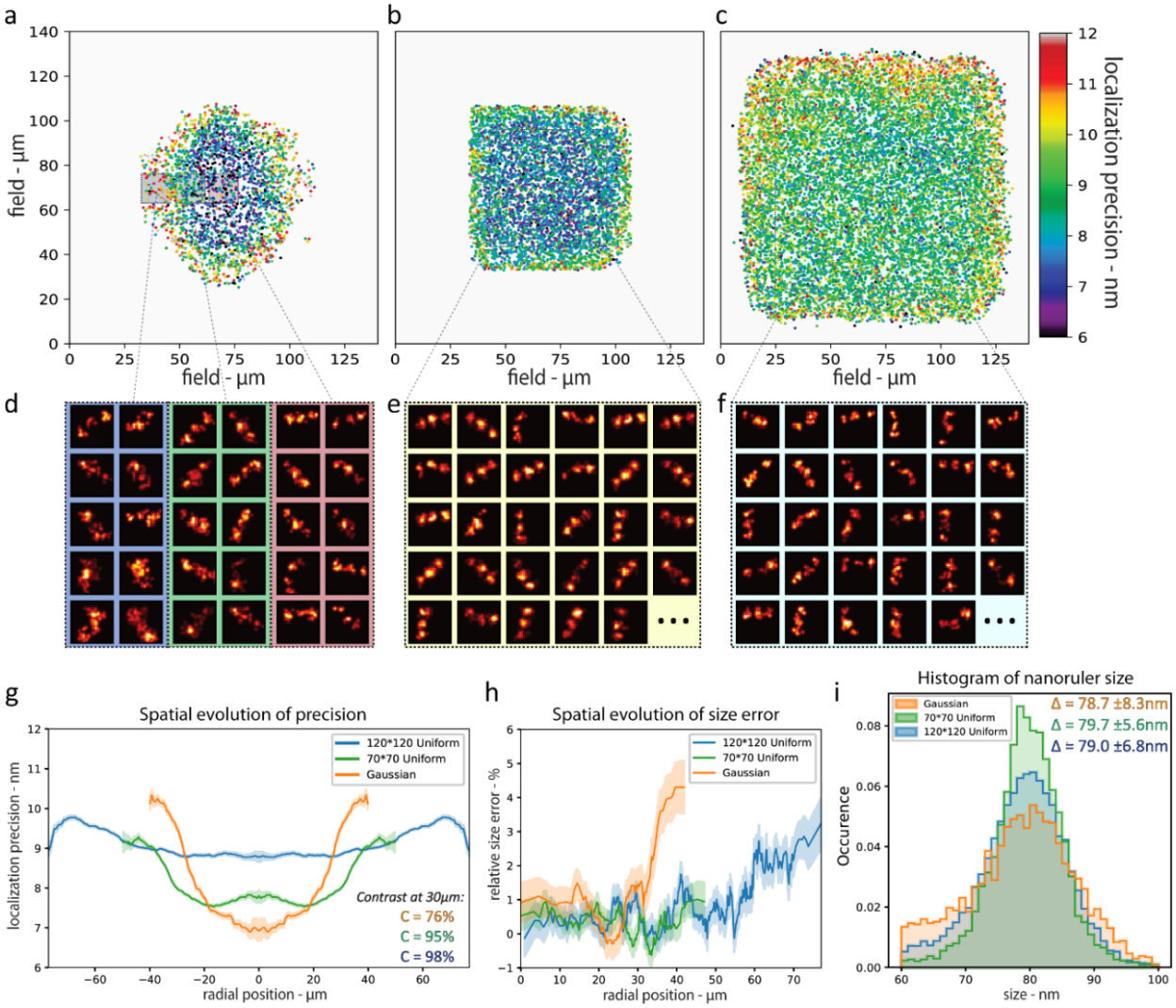

Fig. 3 Nanorulers imaging for localization precision estimation. (a-f) DNA-PAINT imaging of 40 nm spaced 3-spots nanorulers, obtained with Gaussian (left), ASTER small field of view (70 µm x 70 µm, middle), and ASTER large field of view (120 µm x 120 µm, right) illuminations. {a-c} are resulting localization precision maps where each point represents the average precision for one individual nanoruler (3 spots). (d-f) are nanoruler super-resolution images (5 nm pixel size), taken randomly from highlighted areas in (a-c). **(g)** Measured localization precision along FOV radius for each excitation scheme (symmetrized). For each coloured curve, the surrounding transparent curve indicates the standard deviation around the mean precision at a given radius. **(h)** Resulting size estimation error along FOV radius for each excitation scheme. A size error above 0 indicates that the nanoruler spots were measured less than 80 nm apart. Each coloured curve is surrounded by a transparent curve that indicates the standard deviation around the mean size. **(i)** Resulting size measurement histogram for each excitation scheme. The mean and the standard deviation are indicated in the upper right corner.

number of cases where the size was underestimated to 60-70 nm with the Gaussian beam illumination, indicating a poor single molecule regime.

We then turned to STORM experiments on biological samples. Traditionally, STORM demands strong laser power (>2kW/cm²) to drive organic fluorophores into a blinking regime, the stochastic principle STORM relies on. Uniform illumination schemes that illuminate the whole FOV at once have to increase laser power strongly in order to induce a satisfactory blinking regime, with STORM on a 200 µm x 200 µm FOV requiring the use of 1-5 W power lasers[23]. However, as ASTER provides locally high excitation intensity on a short time scale, and a lower global average excitation on longer scales, it may overcome this irradiance threshold rule. We applied ASTER to a direct STORM experiment and found that even with reasonable laser power (<0.3 W at BFP), ASTER was able to induce and maintain a densely-labeled sample in the sparse single molecule regime (<1 molecule in μm^3) on large FOVs (Fig. 4). It appears that the high but intermittent local excitation intensity nonetheless sends most of the molecules in a long-lived dark state efficiently, as is expected for high irradiances[35]. Despite of the non-continuous illumination, the attained single-molecule regime allows for SMLM imaging on a large FOV, where conventional illumination would fail. (Fig. 4a) shows an SMLM image of a COS cell labeled for microtubules and an AF647-coupled secondary antibody. It was obtained using 20,000 frames and a 50 ms camera integration time, using ASTER with 0.3 W laser power, raster scanning a 200 µm x 200 µm FOV (ten lines). The microtubules are well resolved throughout the whole FOV; the zoomed images in (Fig. 4b) show the image quality in several different parts of the image. Analysis of these regions revealed comparable photon distributions, blinking ON-time and localization density during acquisition (Fig. 4c-e). Analysis from regions of an image acquired with a classical Gaussian illumination showed significant differences between the regions, underlining the detrimental effect of inhomogeneous Gaussian illumination (Supplementary Fig. 6a-f). We assessed the experimental image resolution with Fourier Ring Correlation (FRC) analysis[37] (Fig. 4f), and found similar resolutions for each region, from 37

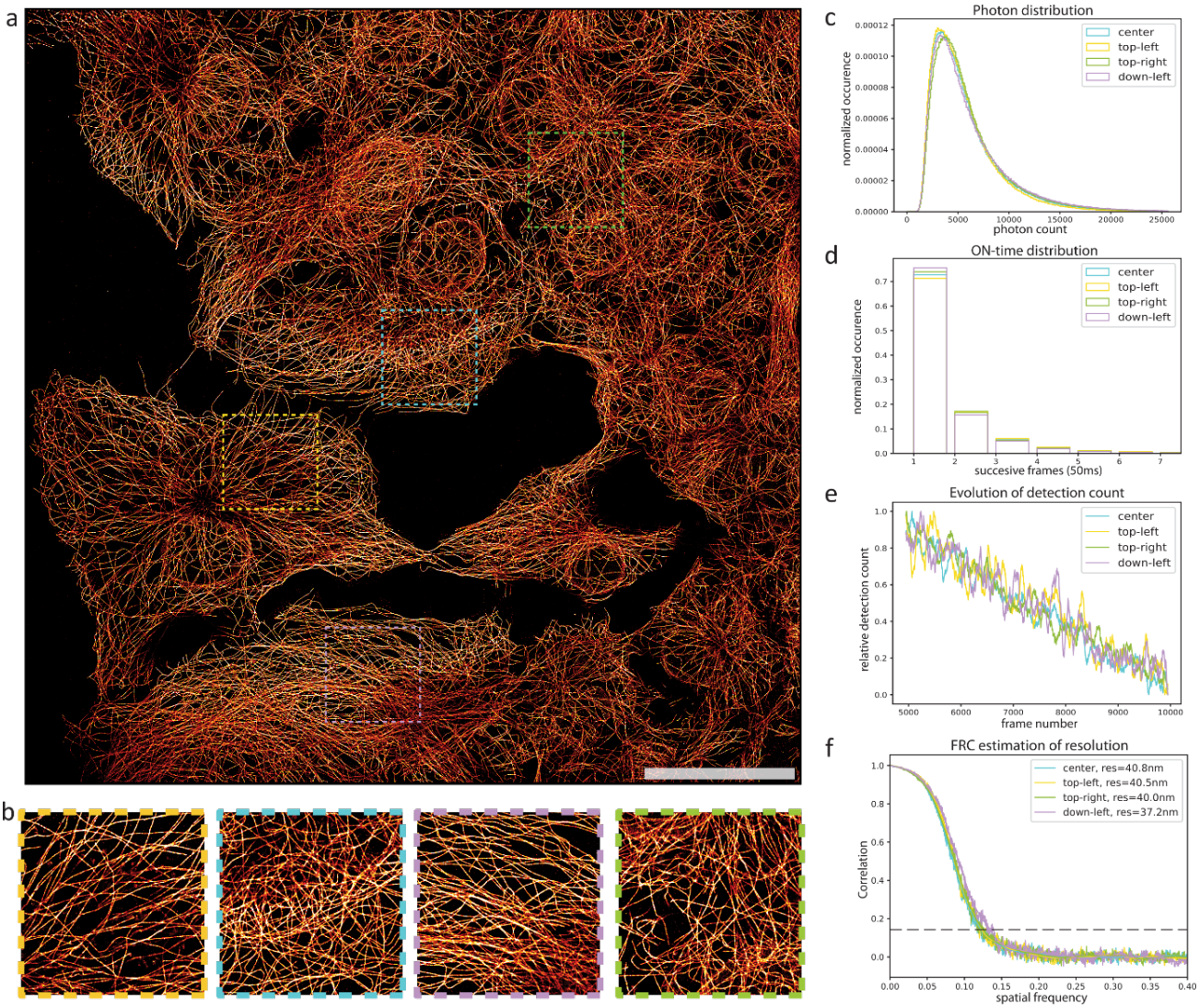

Fig. 4 STORM imaging using ASTER. (a-b) ASTER STORM imaging of COS-7 cells labeled for microtubules and an AF647-coupled secondary antibody, FOV size 200 µm x 200 µm, 20,000 frames at 20 fps. Excitation consisted in a ten-line scan with a laser power of 250 mW at the BFP. (b) shows zoomed views of highlighted areas in (a). Scalebar 50 µm. **(c)** Photon count distribution histogram for highlighted areas in (a). **(d)** Blinking ON-time distribution for highlighted areas in (a), expressed in number of successive frames (50 ms camera integration time). **(e)** Temporal evolution of detection count for highlighted areas in (a). **(f)** FRC estimation of resolution for highlighted areas in (a).

to 40 nm. This confirms ASTER's ability to obtain uniform blinking and resolution on large 200 µm x 200 µm FOVs in STORM. Noteworthy, this FOV was obtained using a reasonable laser power (250 mW at the BFP). ASTER thus is compatible with both DNA-PAINT and STORM experiments even with laser typically used currently on SMLM microscopes. Camera chip and pixel size requirements typically limit the FOV to ~ 220 µm x 220 µm, but the homogeneity of ASTER-obtained images allows to easily extend this by stitching multiple views. We combined four STORM images with minimal overlap, resulting in a 300 µm x 300 µm image (Supplementary Fig. 7a-b). Stitching results in minimal artefacts in the overlapping edge areas (Supplementary Fig. 7c) due to the sharp flat profile of ASTER.

As ASTER homogenously illuminates large FOVs, it extends the possibility of quantitative analysis of nanoscopic structures to whole cells or group of cells. To obtain a precise view of a biological structure at the nanoscale, it is crucial to leverage the imaging of a large number of similar structures. This allows to not only obtain their average characteristics, but also the individual variation of these characteristics caused by both biological variability and

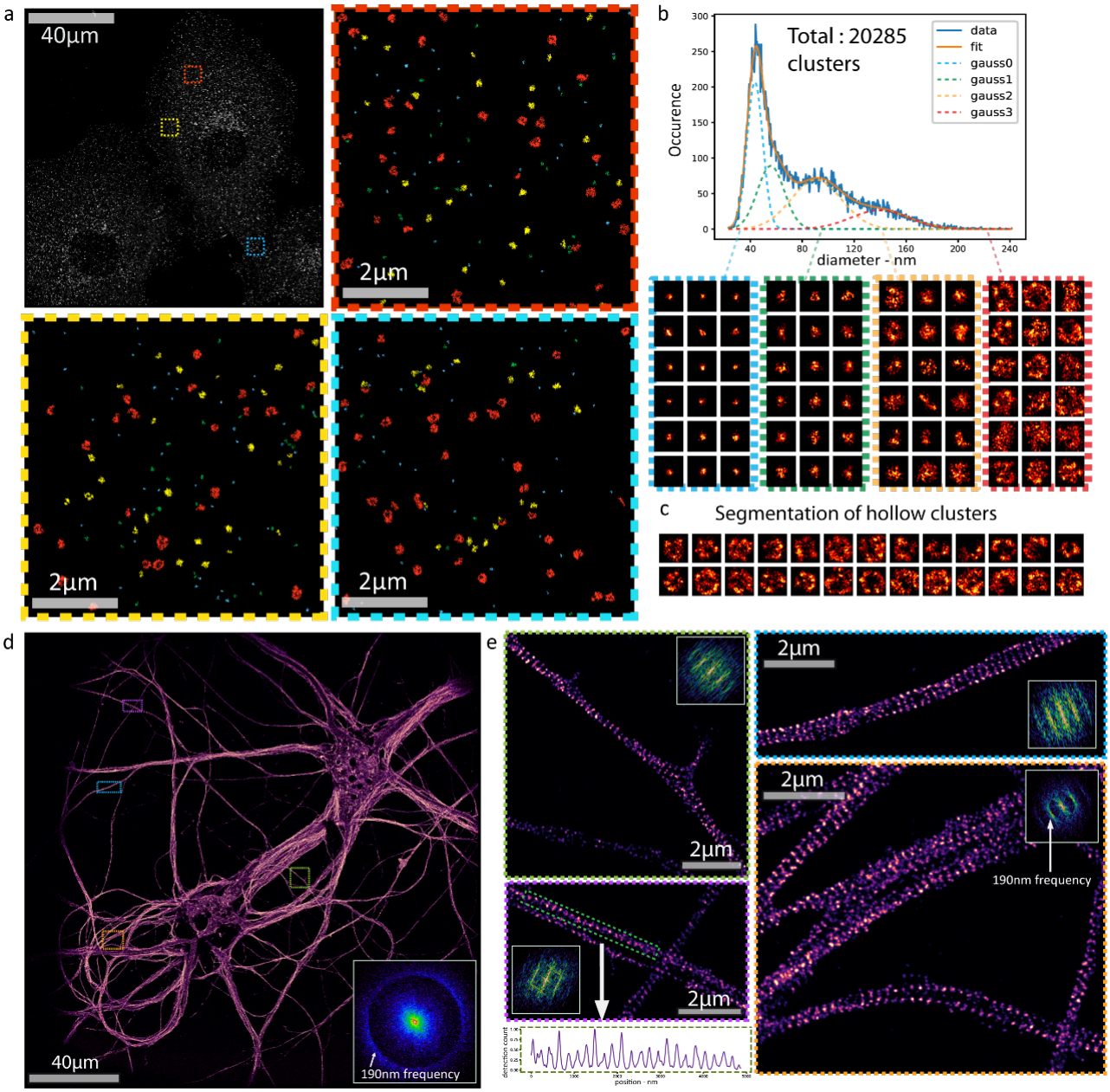

Fig. 5 ASTER applications for single molecule localization microscopy. (a-c) ASTER STORM imaging and cluster analysis of COS-7 cells labeled for clathrin heavy-chain and an AF647-coupled secondary antibody. (a) Final 140 µm x 140 µm image (top left) and close-up views of the highlighted regions (colours encode cluster affiliation). Pixel size is 10 nm. (b) shows the distribution of the diameter of clathrin clusters and highlights four potential populations, that can be fitted with gaussian functions. Below are 5 nm-pixel images of individual clathrin related clusters, each area corresponding to a specific population. (c) shows images (5 nm pixel size) of large, hollow clathrin clusters likely corresponding to large clathrin-coated pits. **(d,e)** ASTER STORM imaging and structural analysis of neurons labeled for β2-spectrin and AF647-coupled secondary antibody. (d) 200 µm x 200 µm STORM image obtained with ASTER (30 nm pixel size). The two-dimensional Fourier transformation (inlet) exhibits a circular frequency pattern corresponding to a ~190 nm periodicity of the staining that is present along all axons. (e) Zoomed views of regions in (d) revealing the periodic cytoskeleton along single axons (pixel size is 10 nm). Insets show their respective two-dimensional Fourier transformation, showing line patterns at corresponding to the known 190 nm periodicity of the axonal spectrin scaffold. bottom left image shows the intensity profile along the highlighted green line, revealing the same the 190 nm periodicity.

imaging uncertainty. We imaged clathrin clusters and clathrin-coated pits by STORM in COS-7 cells (Fig. 5a-c) and applied a cluster analysis. Three COS-7 cells were imaged at once over a large 140 µm x 140 µm FOV, containing approximately 20,000 individual clathrin clusters. In comparison, a classical 30 µm x 30 µm FOV would have yielded ~1,500 pits. The high number of clathrin clusters identified on resolution-uniform images allowed for population estimation from the characteristics of clusters. We picked specific parameters such as diameter and hollowness (see Methods). We were able to distinguish four populations from the cluster diameter distribution, as fitted with normal distributions (Fig. 5b). Small-diameter clusters (below 80 nm, blue and green population of Fig. 5b) likely correspond to pits in formation, while large ones (orange and red populations in Fig. 5b) are likely to be fully assembled pits. We specifically extracted large, hollow clathrin assemblies based on the ratio between the diameter and the spatial dispersion of fluorophores. Hollow clathrin assemblies with diameters of 80-200 nm would be of typical size for the large clathrin-coated pits found in fibroblasts[38]. Interestingly, some large, hollow pits showed more than one fluorescence "holes" within them, suggesting that they are either assemblies of smaller pits or that the fenestration of clathrin cages[39] (pentagon or hexagons of 18 nm side length) can sometimes be resolved.

The large FOV provided by ASTER illumination coupled with large-chip sCMOS cameras also have interesting application for imaging neuronal cells, which grow axons over hundreds of microns in culture. Traditionally, SMLM imaging of axons has been limited to <50 µm segments of axons, impeding the visualization of rare structures and the definition of their large-scale organization[40,41] . We labeled rat hippocampal neurons for β2-spectrin, a protein that forms a periodic sub membrane scaffold along axons by linking actin rings[42,43]. A 200 µm x 200 µm FOV allowed to visualize the dendrites and cell body of two neurons, and a large number of long axonal segments (Fig. 5d). The zoomed views confirm the quality and resolution of the resulting image: the periodic 190 nm organization of axonal spectrin is clearly visible, as confirmed by the corresponding Fourier transform of the images. The Fourier transform of the whole image exhibits a sharp ring at the corresponding frequency, because the banded pattern of β2-spectrins appears in axons running in all directions. On the zoomed images, the β2-spectrin along axons in one direction results in a direction-dependent frequency band on the Fourier transform, corresponding to the 190 nm spacing.

Discussion

We implemented and characterized ASTER, a hybrid scanning and wide-field illumination technique for optimized wide-field fluorescence microscopy and Single Molecule Localization Microscopy (SMLM) over large fields of view (FOV). ASTER generates uniform excitation (> 95% uniformity) combined with a tunable FOV. It outperforms state-of-the-art uniform illumination schemes by its efficiency, flexibility and ability to perform optimized HiLo and TIRF illumination. Indeed, ASTER avoids interference fringes arising from scattered laser light as the scanning temporally averages the instantaneous irradiation profile.

In TIRF, we demonstrated a uniform illumination depth of 100 nm on a 170 µm x 170 µm FOV using 3 µm beads. ASTER-TIRF also allowed to image rat hippocampal neurons labeled for ß2-spectrin over 200 µm x 200 µm, the largest FOV achievable with sCMOS cameras and a 60x magnification. Then SMLM PAINT strategy, which usually requires TIRF or HiLo excitation, also benefits from ASTER: we used nanorulers to demonstrate a uniform localization precision over large FOVs (9 nm over 120 µm x 120 µm), or better resolution on small FOVs (7 nm over 70 µm x 70 µm), while imaging with conventional collimated gaussian beam suffers from significant drop in precision at the edges of the FOV (7-11 nm over 40 µm x 40 µ m). This translates into more precise quantitative analyses: for the three-spot nanorulers, a sharper estimation of the ruler length was obtained thanks to the larger FOV (higher number of objects analyzed) and constant resolution (better precision of each object's measurement). (better precision of each object's measurement).

ASTER is also a particularly efficient excitation method for STORM imaging experiments. Against common belief that driving fluorophores in an efficient single molecule regime requires a strong continuous irradiance (~2 kW/cm^2), we demonstrated that our scanned scheme could obtain uniform blinking dynamics at lower mean irradiance (< 0.5 kW/cm^2) over a large 200 µm x 200 µm FOV, alleviating the need for expensive and dangerous high-power lasers. We further demonstrate the usefulness of precise SMLM over large field of view for imaging biological samples. We were able to measure the periodic 190 nm organization of axonal spectrin on several long axon segments from rat hippocampal neurons. Fourier transforms showed that the periodicity is consistent on the whole image, as well as on distinct regions. The advantages of ASTER for analyzing cluster-like object were also demonstrated on the example of clathrin-coated pits in COS-7 cells: we were able to image multiple cells on a large FOV, thereby increasing the number of identified clusters by a factor of 20 compared to the FOV of a typical STORM acquisition. This allowed detailed cluster analysis, revealing distinct subpopulations in the diameter distribution. The observed populations fall well in place with reported sizes of assembling clathrin-coated pits (diameter < 90 nm) and functional coated pits, capable of endocytosis (90 - 150 nm diameter)

ASTER can be combined with stitching schemes, alternative objectives and camera chips to cover even wider FOV. In SMLM, the field is regularly limited to a maximum of 200 µm x 200 µm, however in classical widefield microscopy ASTER can be coupled with smaller magnification objectives to image larger FOVs and would be a great choice for imaging structures on larger scales. We conclude that ASTER represents a versatile and innovative

tool, especially suited for SMLM. It exhibits robust uniformity and reliability, as well as adaptability to variable FOV sizes. Further uses of ASTER include adapting the field illumination side to speed up imaging in STORM[44] and coupling with improved detection schemes, such as multicolour imaging or strategies to encode axial information[45,46]. The resulting uniformity may be used for demultiplexing or stoichiometry experiments[47,48], as well as in buffer characterization and other fields such as photolitography. Finally, ASTER has potential applications in non-uniform excitation schemes, such as using smaller beam to concentrate power, exciting specific areas of a sample or creating a patterned irradiance on complex samples by using adaptive scanning strategies.

Acknowledgements

We acknowledge people who provided valuable advice and support in the course of this study; particularly P. Jouchet and C. Cabriel. We thank S. Vassilopoulos for discussions about clathrin organization in cells. M. Bardou and F. Boroni-Rueda helped with cell culture and labelling. C. Hubert and E. Fort provided the lasers and galvanometers.

Author contributions

A.M., N.B. and S.L.-F. conceived the project. All authors contributed to the writing and editing of the manuscript. K.F and C.L provided neuronal samples. Experimental acquisitions and analyses were performed by A.M.

Competing financial interests

N.B. and S.L.F. are shareholders in Abbelight.

Methods

Optical setup

We used a Nikon Eclipse Ti inverted microscope with a Nikon Perfect Focus System. The excitation was performed with a ELERA laser (638 nm) from ERROL. Both excitation and detection went through the left camera port of the microscope to prevent undesired cropping. The fluorescence was collected through an Olympus x60 1.49NA oil immersion objective, a relay-system, and recorded on a 2048*2048 pixel sCMOS camera (Orca-Flash 4 v3, Hamamatsu). The optical pixel size was approximately 108 nm.

Calibration samples preparation

Beads: Beads are 3 µm radius biotin-polystyrene microspheres (Kisker Biotech,PC-B-3.0) on which we attached Alexa Fluor (AF) 647 functionalized with streptavidin (Life Technologies, S21374).(ref du papier) We prepared a solution containing 500 µL of water, 500 µL of PBS, 35 µL of microsphere solution, and 0.34 µL of AF647. This solution was centrifuged 20 min at 13.4 krpm. The liquid was then removed and replaced with 100 µL of PBS, followed by 5 minutes vortexing to dissolve the deposit. 50 µL of the final solution was then pipetted on to a glass coverslip and left for 20 min so that beads would have time to deposit. Finally, we added 500 µL of imaging dSTORM buffer (dSTORM smart kit, Abbelight). Images were taken at low laser power and integrated over 100 ms, for an ASTER scan period of 50 ms.

Nanorulers: Nanorulers (Gattaquant, PAINT-40R) consist in 3 aligned spots, separated by 40 nm and are labelled with ATTO655 fluorophores. They were all imaged under 100 ms integrations times, with excitations consisting in 200mW power in a constant TIRF excitation.

Fluorescence immunolabeling

Neuronal culture: Rat hippocampal neurons in culture were prepared according to the Banker protocol[49]. Briefly, E18 Wistar rat embryo hippocampi (Janvier labs) were dissected, then cells were homogenized and plated in B27-containing Neurobasal medium on Poly-L-Lysine treated #1.5H glass coverslips (Marienfeld, VWR) to a density of 4000 cells per cm^2. The neurons were then co-cultured with glia cells - neuron coverslip upside down, separated from the glia on the bottom of the petri dish by wax beads. Mature neurons were fixed after 14 days in culture. All procedures followed the guidelines from European Animal Care and Use Committee (86/609/CEE) and were approved by local ethics committee (agreement D13-055-8).

Immunolabeling of neurons was performed as described recently for optimized SMLM sample preparation[4745] Neurons were fixed using 4% paraformaldehyde (Delta Microscopie, #15714) and 4% (w/v) sucrose in PEM buffer (80 mM PIPES, 2 mM $MgCl_2$, 5 mM EGTA, pH 6.8) for 20 minutes at RT. Cells were then rinsed with 0.1 M phosphate buffer. Blocking and permeabilization were performed in ICC buffer (0.2% (v/v) gelatin, 0.1% Triton X-100 in phosphate buffer) for 2 hours on a rocking table. Primary antibodies diluted in ICC were incubated overnight at 4°C, rinsed and incubated with the secondary antibodies diluted in ICC for one hour at room temperature. After a final rinse with ICC and phosphate buffer, the samples were stored in phosphate buffer with 0.02 % (w/v) sodium azide before imaging. For immunolabeling, we used mouse anti β2-spectrin (BD Sciences, #612563, 2.5 µg/ml) and donkey anti-mouse AF647 (ThermoFisher, #A31571, 6.67 µg/ml).

Cell line culture: COS-7 cells were grown in DMEM with 10% FBS, 1% L-glutamin and 1% penicillin / streptomycin (Life Technologies) at 37°C and 5% CO2 in a cell culture incubator. Two days later, they were plated at medium confluence on cleaned, round 25 mm diameter high resolution 1.5'' glass coverslips (Marienfield, VWR). After 24 hours, the cells were washed three times with PHEM solution (60 mM PIPES, 25 mM HEPES, 5 mM EGTA and 2 mM Mg acetate adjusted to pH 6.9 with 1 M KOH). For preparation of STORM microtubule imaging, we added an extraction solution (0.25% Triton, 0.025% Glutaraldehyde in PEM) for 30 s then a fixation solution (0.5% glutaraldehyde, 0.5% Triton in PEM) for 12 min followed by a reduction solution ($NaBH_4$: 0,1 % in PBS 1X) for 7 minutes. For clathrin we directly fixed with a 4% PFA solution. Extraction and fixation solutions were pre-warmed at 37°C. Cells were then washed 3 times in PBS before being blocked for 15 min in PBS + 1% BSA + 0.1% Triton. Labelling was

performed in a similar solution with intermediary washing steps. α-tubulin (Sigma Aldrich, T6199) and clathrin heavy-chain (Abcam, ab2731) primary antibodies were conjugated with Rb-AF647 (Life Technologies, A21237). Cells were finally post-fixed for 16 minutes in 3.7% Formaldehyde and reduced for 10 min with NH_4Cl (3mg/mL).

Imaging

Wide-field fluorescence imaging: TIRF imaging on neuronal sample was done at 200 ms integration times and a low 30 mW laser power. Samples consisted in β2-spectrin labelled with AF647.

STORM imaging: STORM imaging on COS-7 cells (microtubules and clathrin) and neurons (ß2-spectrin) was performed using an oblique epifluorescence illumination configuration. A STORM buffer (Abbelight Smart kit) was used to induce most of the molecules in a dark state. The sample was lit with laser powers of approximately 250 mW in the objective BFP. Data acquisition was performed at 50 ms exposure time for an ASTER excitation scanning ten lines in 50 ms. The acquisition was performed and analyzed using the Nemo software (Abbelight). Localization consisted in a wavelet segmentation after median background removal, followed by gaussian fits of individual point spread functions. Sample was drift-corrected using a classical redundant cross-correlation algorithm.

Image processing and analysis

Analysis and measurement of beads radius from (Fig. 2), nanoruler from (Fig. 3) and clathrin from (Fig. 5) were done in Python 3.7; the code is available online.

Beads: Beads (microspheres) were detected on the TIRF image: we first applied a Laplace filter from scipy library, followed by low-pass filtering in Fourier space to diminish noise. Use of an intensity threshold then proved sufficient to efficiently detect individual beads. Peaks positions were measured via local extrema algorithms.

Nanorulers: Nanorulers analysis focused on resulting X,Y coordinates. A preliminary DBscan clustering was used to localize and filter out lonesome localizations. Then a more precise DBscan was used to distinguish individual groups of three-spots and associate a number to each of them. Parameters of this secondary scan were: epsilon=50 nm and minimum number of points mpts=10. DBscan typically consider core points, which are point with at least mpts neighbor in a surrounding epsilon radius, then iteratively add adjacent points. With these parameters, adjacent spots belonging to a similar nanoruler array were grouped together, while unwanted associations of adjacent nanorulers were minimized. For each group, a Gaussian Mixture Model (GMM) clustering was used to estimate parameters from three gaussian distribution. GMM also estimates the mean and standard deviation of each spot, which allowed for size estimation and localization precision measurements. Nanorulers with too few points or extraordinary distance estimations were thrown away.

Clathrin clusters: Clathrin analysis was primarily performed via a DBscan clustering, with an epsilon parameter of 35 nm and a minimum number of points of 25. This clustering method localized each individual cluster of close points. For each of these cluster we calculated several parameters, such as the mean position and the effective diameter, Feret's diameter, the hollowness, the angle of orientation and eccentricity. Effective diameter and mean position were calculated by minimizing radial dispersion among points. Hollowness consisted in the ratio between the mean radius value, divided by the standard deviation of radius, and was found to be rather independent of the size of the cluster. Among all parameters, the diameter and the hollowness proved to be the most relevant in term of describing cluster distributions.

Data availability

SMLM large data files (>20Go) are available from the corresponding author on reasonable request. Other data files are available on Zenodo (DOI: 10.5281/zenodo.3814322) as well as related analysis code.

Code availability

Code is available online on Github at the following link: https://github.com/AdrienMau/ASTER_code and Zenodo (DOI: 10.5281/zenodo.3814322).

References

1. Tokunaga, M., Imamoto, N. & Sakata-Sogawa, K. Highly inclined thin illumination enables clear single-molecule imaging in cells. *Nat. Methods* **5**, 159–161 (2008).

2. Nakata, T. & Hirokawa, N. Microtubules provide directional cues for polarized axonal transport through interaction with kinesin motor head. *J. Cell Biol.* **162**, 1045–1055 (2003).

3. Guo, Y. *et al.* Visualizing Intracellular Organelle and Cytoskeletal Interactions at Nanoscale Resolution on Millisecond Timescales. *Cell* **175**, 1430-1442.e17 (2018).

4. Stout, A. L. & Axelrod, D. Evanescent field excitation of fluorescence by epi-illumination microscopy. *Appl. Opt.* **28**, 5237 (1989).

5. Axelrod, D. Cell-substrate contacts illuminated by total internal reflection fluorescence. *J. Cell Biol.* **89**, 141–145 (1981).

6. Stock, K. *et al.* Variable-angle total internal reflection fluorescence microscopy (VA-TIRFM): realization and application of a compact illumination device. *J. Microsc.* **211**, 19–29 (2003).

7. Konopka, C. A. & Bednarek, S. Y. Variable-angle epifluorescence microscopy: a new way to look at protein dynamics in the plant cell cortex. *Plant J.* **53**, 186–196 (2008).

8. van 't Hoff, M., de Sars, V. & Oheim, M. A programmable light engine for quantitative single molecule TIRF and HILO imaging. *Opt. Express* **16**, 18495 (2008).

9. Mattheyses, A. L., Shaw, K. & Axelrod, D. Effective elimination of laser interference fringing in fluorescence microscopy by spinning azimuthal incidence angle. *Microsc. Res. Tech.* **69**, 642–647 (2006).

10. Fiolka, R., Belyaev, Y., Ewers, H. & Stemmer, A. Even illumination in total internal reflection fluorescence microscopy using laser light. *Microsc. Res. Tech.* **71**, 45–50 (2008).

11. Boulanger, J. *et al.* Fast high-resolution 3D total internal reflection fluorescence microscopy by incidence angle scanning and azimuthal averaging. *Proc. Natl. Acad. Sci.* **111**, 17164–17169 (2014).

12. Schreiber, B., Elsayad, K. & Heinze, K. G. Axicon-based Bessel beams for flat-field illumination in total internal reflection fluorescence microscopy. *Opt. Lett.* **42**, 3880 (2017).

13. Almada, P., Culley, S. & Henriques, R. PALM and STORM: Into large fields and high-throughput microscopy with sCMOS detectors. *Methods* **88**, 109–121 (2015).

14. Betzig, E. *et al.* Imaging Intracellular Fluorescent Proteins at Nanometer Resolution. *Science* **313**, 1642–1645 (2006).

15. Hess, S. T., Girirajan, T. P. K. & Mason, M. D. Ultra-High Resolution Imaging by Fluorescence Photoactivation Localization Microscopy. *Biophys. J.* **91**, 4258–4272 (2006).

16. Rust, M. J., Bates, M. & Zhuang, X. Sub-diffraction-limit imaging by stochastic optical reconstruction microscopy (STORM). *Nat. Methods* **3**, 793–796 (2006).

17. Heilemann, M. *et al.* Subdiffraction-Resolution Fluorescence Imaging with Conventional Fluorescent Probes. *Angew. Chem. Int. Ed.* **47**, 6172–6176 (2008).

18. Heilemann, M., van de Linde, S., Mukherjee, A. & Sauer, M. Super-Resolution Imaging with Small Organic Fluorophores. *Angew. Chem. Int. Ed.* **48**, 6903–6908 (2009).

19. Sharonov, A. & Hochstrasser, R. M. Wide-field subdiffraction imaging by accumulated binding of diffusing probes. *Proc. Natl. Acad. Sci.* **103**, 18911–18916 (2006).

20. Douglass, K. M., Sieben, C., Archetti, A., Lambert, A. & Manley, S. Super-resolution imaging of multiple cells by optimized flat-field epi-illumination. *Nat. Photonics* **10**, 705–708 (2016).

21. Khaw, I. *et al. Flat-field illumination for quantitative fluorescence imaging*. http://biorxiv.org/lookup/doi/10.1101/297242 (2018) doi:10.1101/297242.

22. Rowlands, C. J., Ströhl, F., Ramirez, P. P. V., Scherer, K. M. & Kaminski, C. F. Flat-Field Super-Resolution Localization Microscopy with a Low-Cost Refractive Beam-Shaping Element. *Sci. Rep.* **8**, 5630 (2018).

23. Stehr, F., Stein, J., Schueder, F., Schwille, P. & Jungmann, R. Flat-top TIRF illumination boosts DNA-PAINT imaging and quantification. *Nat. Commun.* **10**, 1268 (2019).

24. Zhao, Z., Xin, B., Li, L. & Huang, Z.-L. High-power homogeneous illumination for super-resolution localization microscopy with large field-of-view. *Opt. Express* **25**, 13382–13395 (2017).

25. Deschamps, J., Rowald, A. & Ries, J. Efficient homogeneous illumination and optical sectioning for quantitative single-molecule localization microscopy. *Opt. Express* **24**, 28080 (2016).

26. Kwakwa, K. *et al.* easySTORM: a robust, lower-cost approach to localisation and TIRF microscopy. *J. Biophotonics* **9**, 948–957 (2016).

27. Chen, S.-Y., Bestvater, F., Schaufler, W., Heintzmann, R. & Cremer, C. Patterned illumination single molecule localization microscopy (piSMLM): user defined blinking regions of interest. *Opt. Express* **26**, 30009 (2018).

28. Ramachandran, S., Cohen, D. A., Quist, A. P. & Lal, R. High performance, LED powered, waveguide based total internal reflection microscopy. *Sci. Rep.* **3**, 2133 (2013).

29. Diekmann, R. *et al.* Chip-based wide field-of-view nanoscopy. *Nat. Photonics* **11**, 322–328 (2017).

30. Archetti, A. *et al.* Waveguide-PAINT offers an open platform for large field-of-view super-resolution imaging. *Nat. Commun.* **10**, 1267 (2019).

31. Bourg, N. *et al.* Direct optical nanoscopy with axially localized detection. *Nat. Photonics* **9**, 587–593 (2015).

32. Devauges, V. *et al.* Homodimerization of Amyloid Precursor Protein at the Plasma Membrane: A homoFRET Study by Time-Resolved Fluorescence Anisotropy Imaging. *PLoS ONE* **7**, e44434 (2012).

33. Michelson. Studies in optics. in *Studies in optics* (1927).

34. Mattheyses, A. L. & Axelrod, D. Direct measurement of the evanescent field profile produced by objective-based total internal reflection fluorescence. *J. Biomed. Opt.* **11**, 014006 (2006).

35. Cabriel, C., Bourg, N., Dupuis, G. & Lévêque-Fort, S. Aberration-accounting calibration for 3D single-molecule localization microscopy. *Opt. Lett.* **43**, 174 (2018).

36. Ester, M., Kriegel, H.-P. & Xu, X. A Density-Based Algorithm for Discovering Clusters in Large Spatial Databases with Noise. 6.

37. Banterle, N., Bui, K. H., Lemke, E. A. & Beck, M. Fourier ring correlation as a resolution criterion for super-resolution microscopy. *J. Struct. Biol.* **183**, 363–367 (2013).

38. Heuser, J. Three-dimensional visualization of coated vesicle formation in fibroblasts. *J. Cell Biol.* **84**, 560–583 (1980).

39. Lampe, M., Vassilopoulos, S. & Merrifield, C. Clathrin coated pits, plaques and adhesion. *J. Struct. Biol.* **196**, 48–56 (2016).

40. Leterrier, C. *et al.* Nanoscale Architecture of the Axon Initial Segment Reveals an Organized and Robust Scaffold. *Cell Rep.* **13**, 2781–2793 (2015).

41. Ganguly, A. *et al.* A dynamic formin-dependent deep F-actin network in axons. *J. Cell Biol.* **210**, 401–417 (2015).

42. Xu, K., Zhong, G. & Zhuang, X. Actin, Spectrin, and Associated Proteins Form a Periodic Cytoskeletal Structure in Axons. *Science* **339**, 452–456 (2013).

43. Leterrier, C., Dubey, P. & Roy, S. The nano-architecture of the axonal cytoskeleton. *Nat. Rev. Neurosci.* **18**, 713–726 (2017).

44. Lin, Y. *et al.* Quantifying and Optimizing Single-Molecule Switching Nanoscopy at High Speeds. *PLOS ONE* **10**, e0128135 (2015).

45. Huang, B., Wang, W., Bates, M. & Zhuang, X. Three-Dimensional Super-Resolution Imaging by Stochastic Optical Reconstruction Microscopy. *Science* **319**, 810–813 (2008).

46. Cabriel, C. *et al.* Combining 3D single molecule localization strategies for reproducible bioimaging. *Nat. Commun.* **10**, 1980 (2019).

47. Bossi, M. *et al.* Multicolor Far-Field Fluorescence Nanoscopy through Isolated Detection of Distinct Molecular Species. *Nano Lett.* **8**, 2463–2468 (2008).

48. Fricke, F., Beaudouin, J., Eils, R. & Heilemann, M. One, two or three? Probing the stoichiometry of membrane proteins by single-molecule localization microscopy. *Sci. Rep.* **5**, 14072 (2015).

49. Kaech, S. & Banker, G. Culturing hippocampal neurons. *Nat. Protoc.* **1**, 2406–2415 (2006).

50. Vassilopoulos, S., Gibaud, S., Jimenez, A., Caillol, G. & Leterrier, C. Ultrastructure of the axonal periodic scaffold reveals a braid-like organization of actin rings. *Nat. Commun.* **10**, 5803 (2019).

Supplementary Figures for:

Fast scanned widefield scheme provides tunable and uniform illumination for optimized SMLM on large fields of view

Adrien Mau [1,2]*, Karoline Friedl [2,3], Christophe Leterrier [3], Nicolas Bourg [2] and Sandrine Lévêque-Fort [1]*

[1] Université Paris-Saclay, CNRS, Institut des Sciences Moléculaires d'Orsay, 91405, Orsay, France.
[2] Abbelight, 191 avenue Aristide Briand, Cachan, France.
[3] Aix-Marseille Université, CNRS, INP UMR7051, NeuroCyto, Marseille, France.
* Corresponding authors : adrien.mau@u-psud.fr , sandrine.leveque-fort@u-psud.fr

Supplementary Figure 1: Synthesis of uniform field, effect of beam size

Supplementary Figure 2: Implementation of TIRF and oblique illumination in classical and ASTER excitation schemes

Supplementary Figure 3: Beads for calibrations of optical sectioning

Supplementary Figure 4: EPI and TIRF images of microtubules

Supplementary Figure 5: Workflow analysis of nanoruler images

Supplementary Figure 6: Gaussian illumination effects in single molecule STORM microscopy

Supplementary Figure 7: Stitching of STORM images resulting in a 300 x 300 µm² field of view

Supplementary Figure 8: STORM 120 µm x 120 µm image of neuronal β2-spectrin.

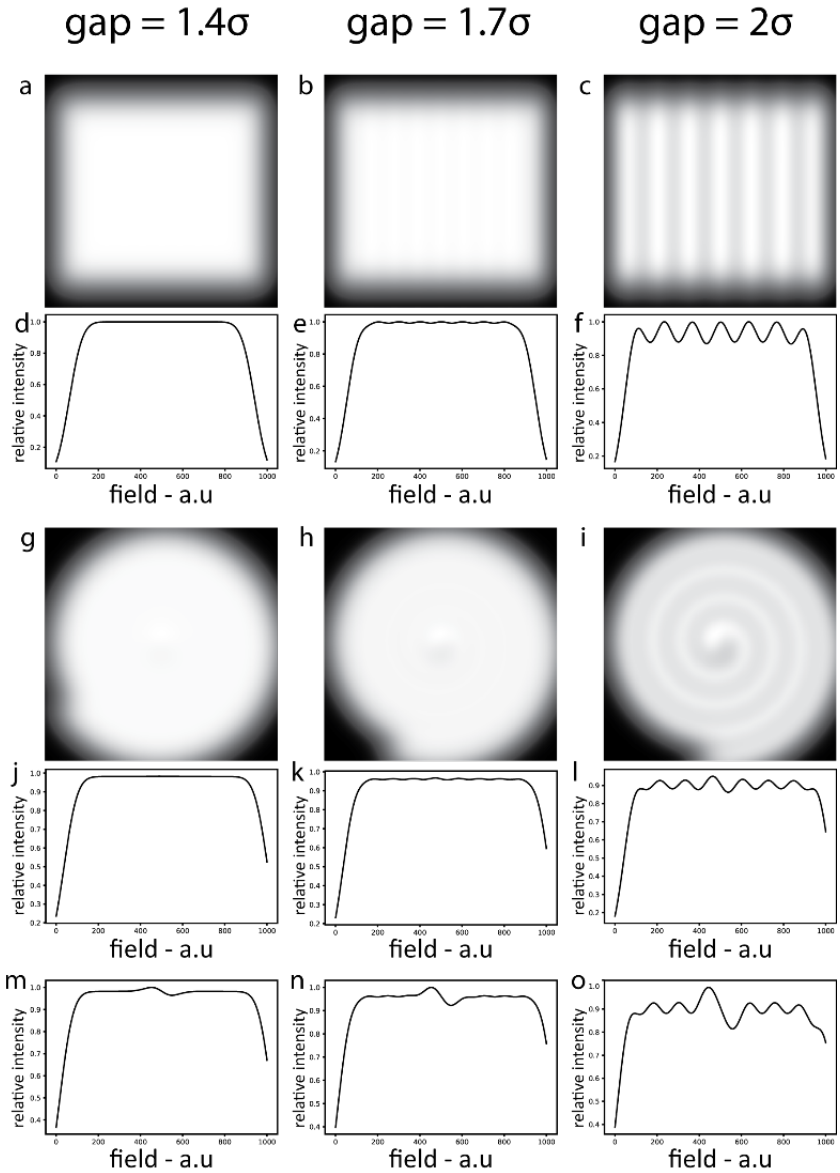

Supplementary Figure 1 Field synthesis with different base gaussian beam size and different scanning patterns. **(a-f)** Raster-scanning path, (a-c) showing a similar scanning path for different beam size, and (d-f) their respective resulting illumination profiles along a horizontal axis. **(g-o)** Scanning of an Archimedes spiral, (g-i) showing a similar scanning path for different beam size, and (j-o) their respective resulting illumination profiles along horizontal (j-l) and vertical (m-o) axes.

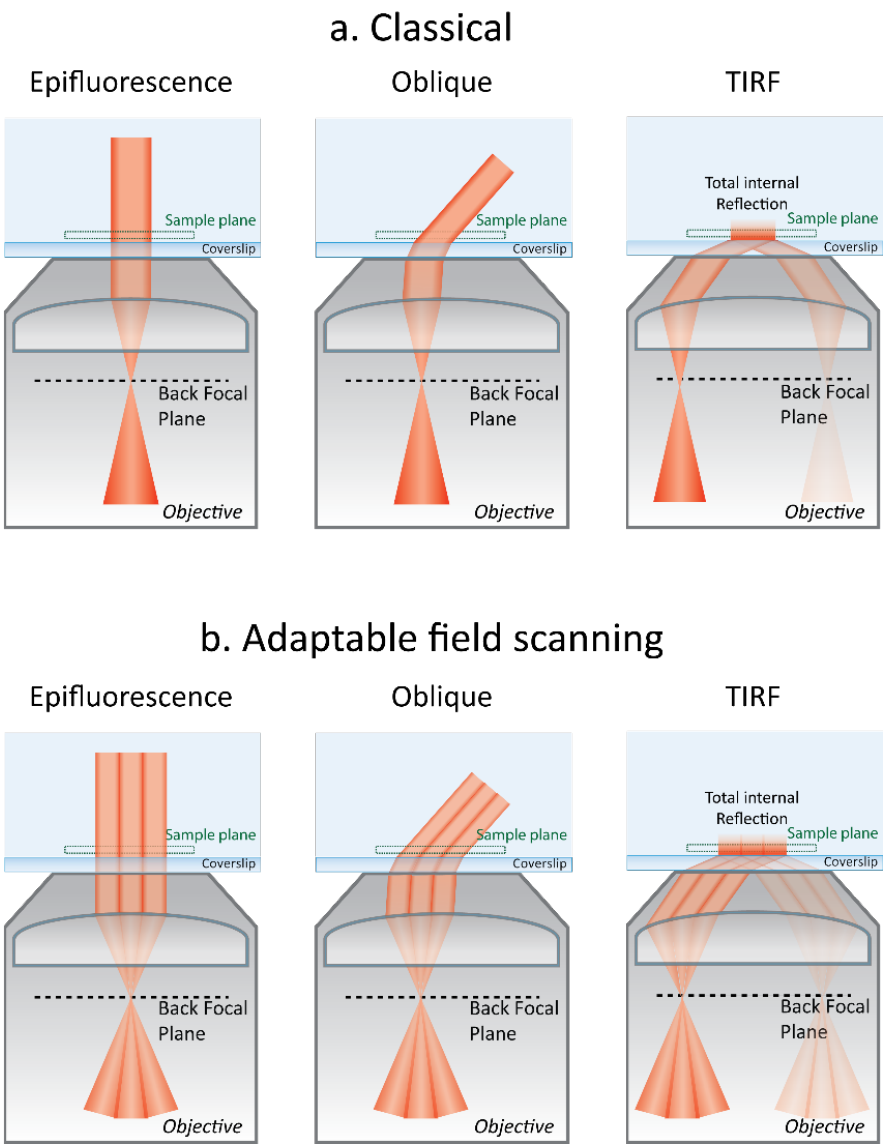

Supplementary Figure 2 Implementation of TIRF and oblique illumination in classical and ASTER excitation schemes. **(a)** Classical configuration in EPI, oblique HiLo and TIRF, from left to right. Each position in the Back Focal Plane coincides with a given output angle. **(b)** ASTER configuration for EPI, oblique HiLo and TIRF, where the scanning effect modifies the effective field of view but does not affect the output angle.

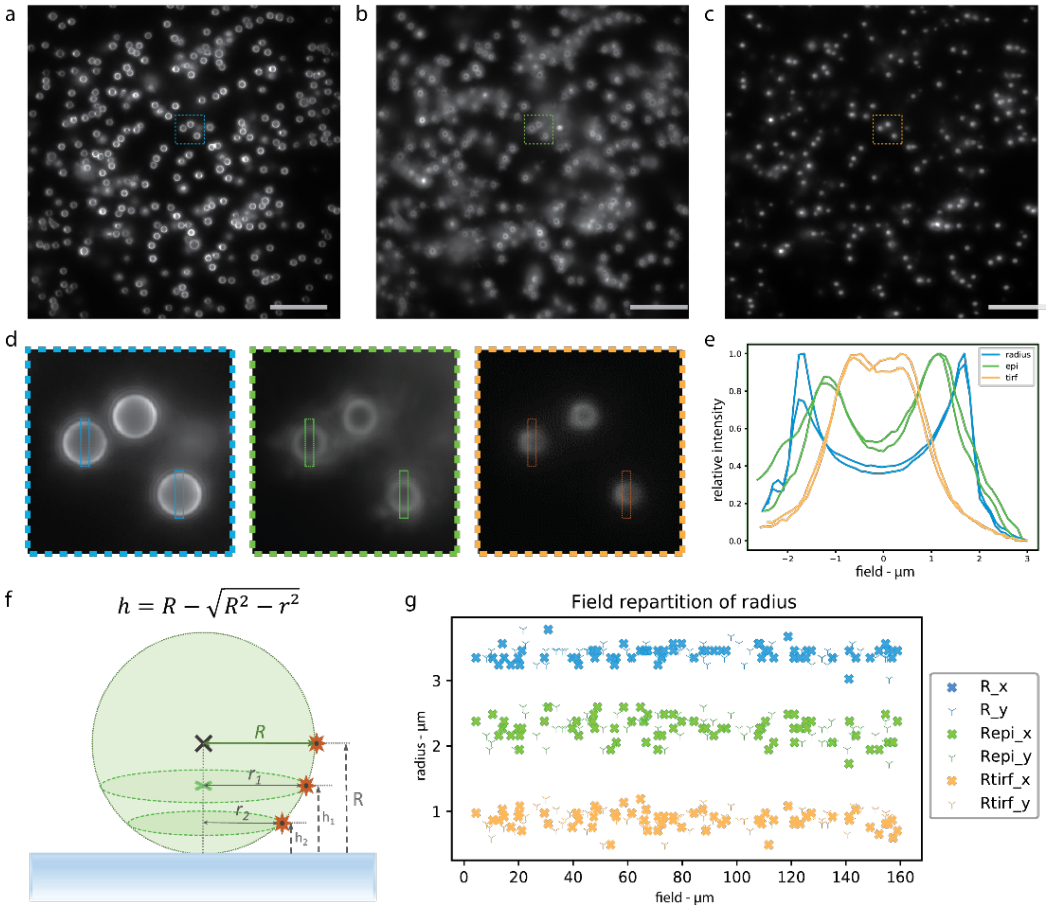

Supplementary Figure 3 Measurement of the effective optical sectioning (excitation and detection) in epi and TIRF using labelled beads. **(a)** Imaging of beads in epi, with focus at the beads median planes. **(b)** Imaging of beads in EPI, with focus at the coverslip. **(c)** Imaging of beads in TIRF, with focus at the coverslip. **(d)** Close up view of highlighted areas in (a-c) showing that each illumination condition results in its own effective bead radius. **(e)** Vertical profiles of highlighted cross-sections in (d).

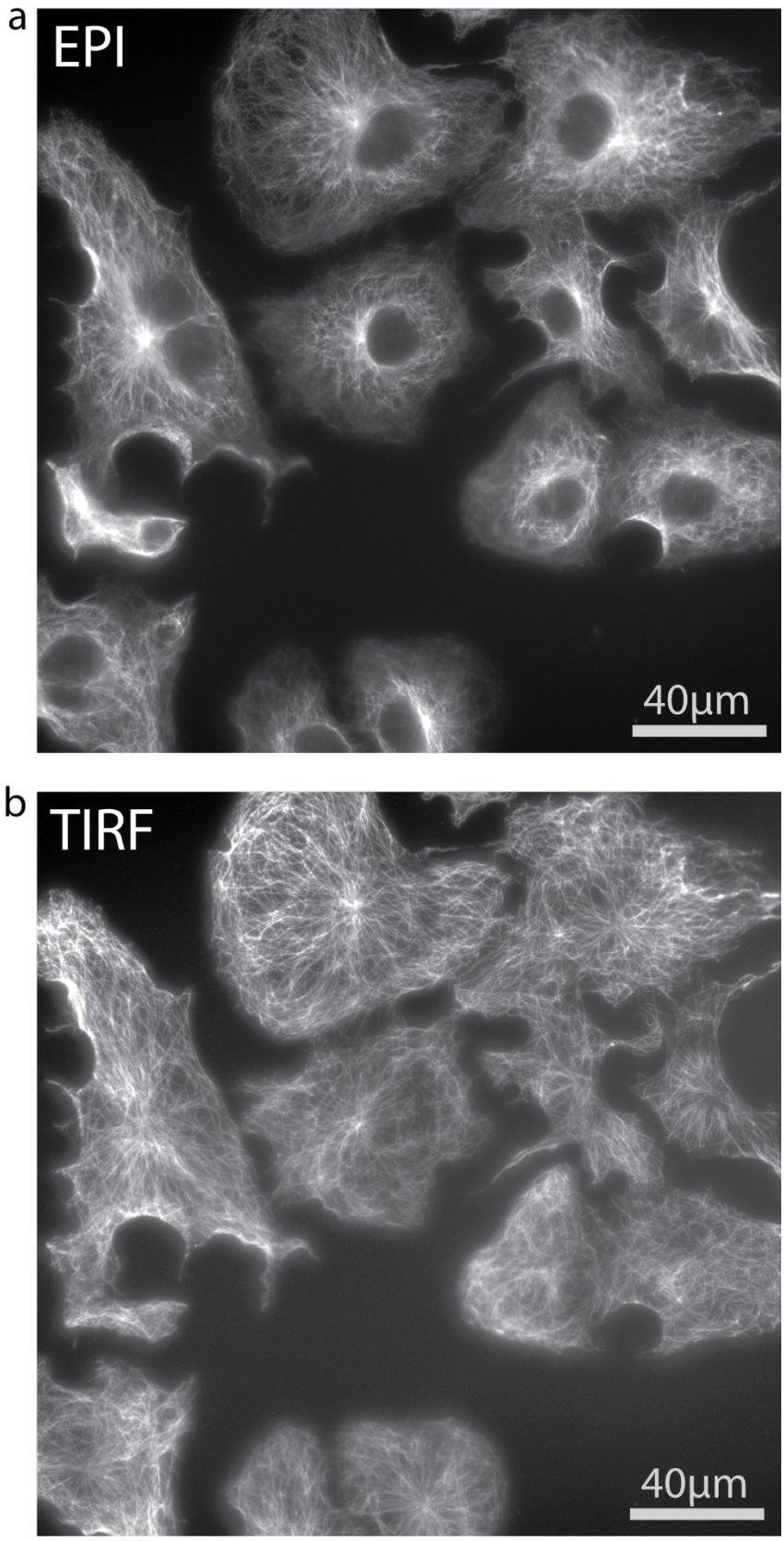

Supplementary Figure 4 Image of COS-7 cells labeled for microtubules and AF647-coupled secondary antibodies. **(a)** EPI image. **(b)** TIRF Image. Scalebars 40 µm.

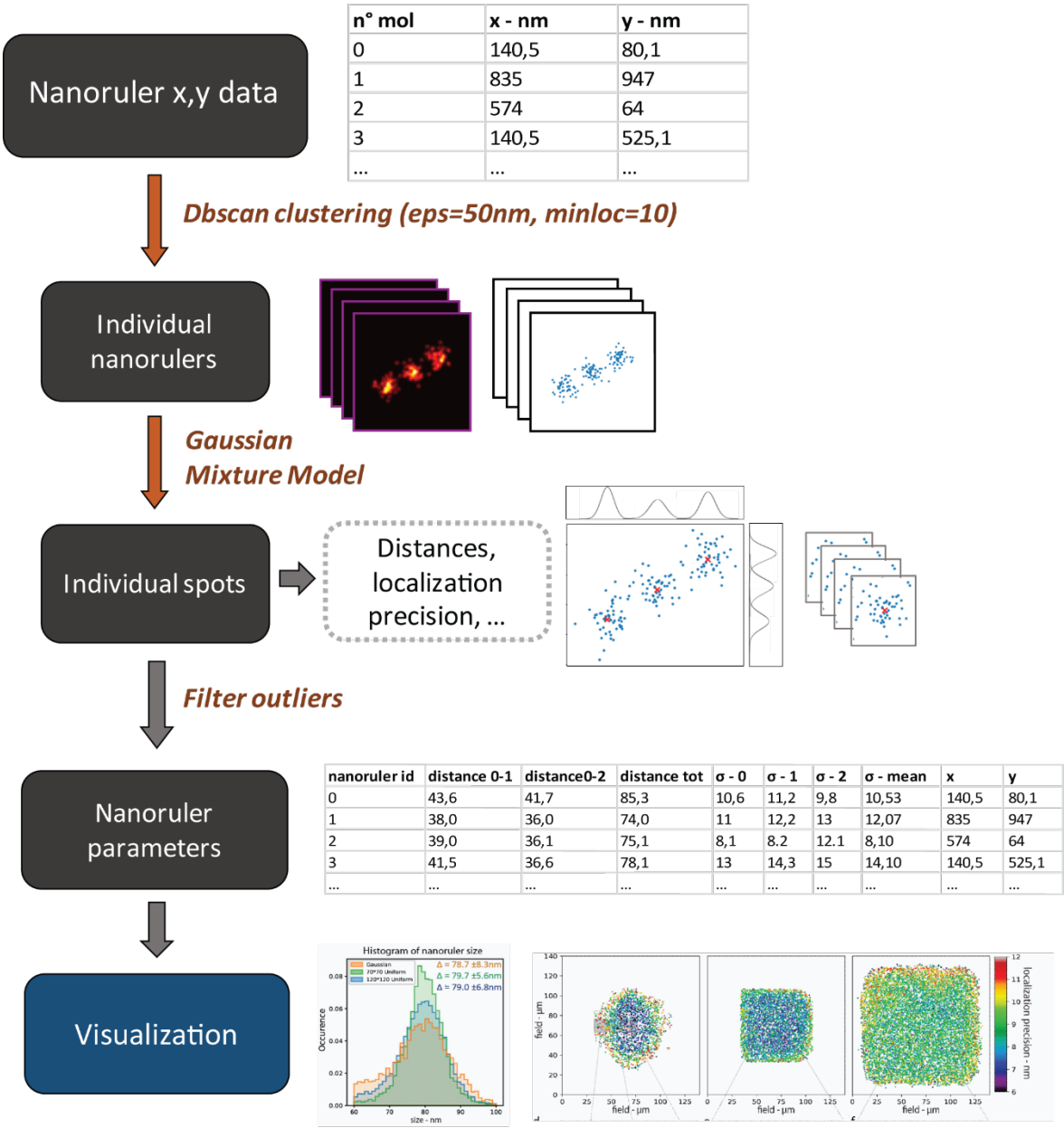

Supplementary Figure 5 Workflow Analysis for three spot nanorulers. (See Methods). A DBscan isolate each individual nanoruler, consisting of three aligned spots, each separated by 40nm. For each individual nanoruler a gaussian mixture model fit the localization point cloud with three 2D normal distribution. This result in mean and standard deviation for each spot that allows for measurement of nanoruler sizes, and estimation of localization precision for each nanoruler.

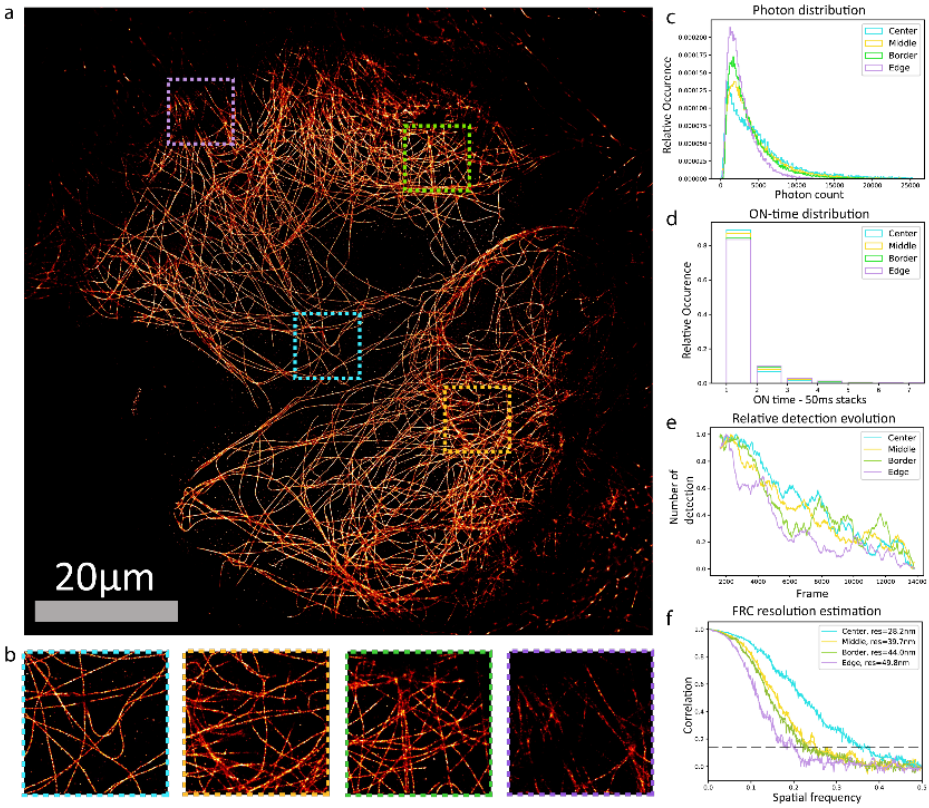

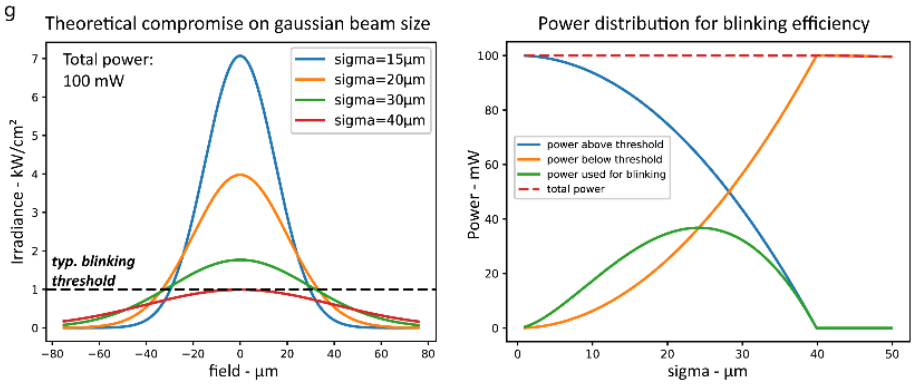

Supplementary Figure 6 Resulting image and blinking kinetics in single molecule STORM microscopy under a classical Gaussian excitation. **(a-b)** Gaussian STORM imaging of COS-7 cells labeled for microtubules using AF647-coupled antibodies. Detection was done on 20000 frames at 20 fps. (b) shows close up views of highlighted areas in (a). **(c)** Photon count distribution histogram for highlighted areas in (a). **(d)** Blinking ON-time distribution for highlighted areas in (a), expressed in number of frames (50 ms). **(e)** Temporal evolution of detection count for highlighted areas in (a). **(f)** FRC estimation of resolution for highlighted areas in (a).

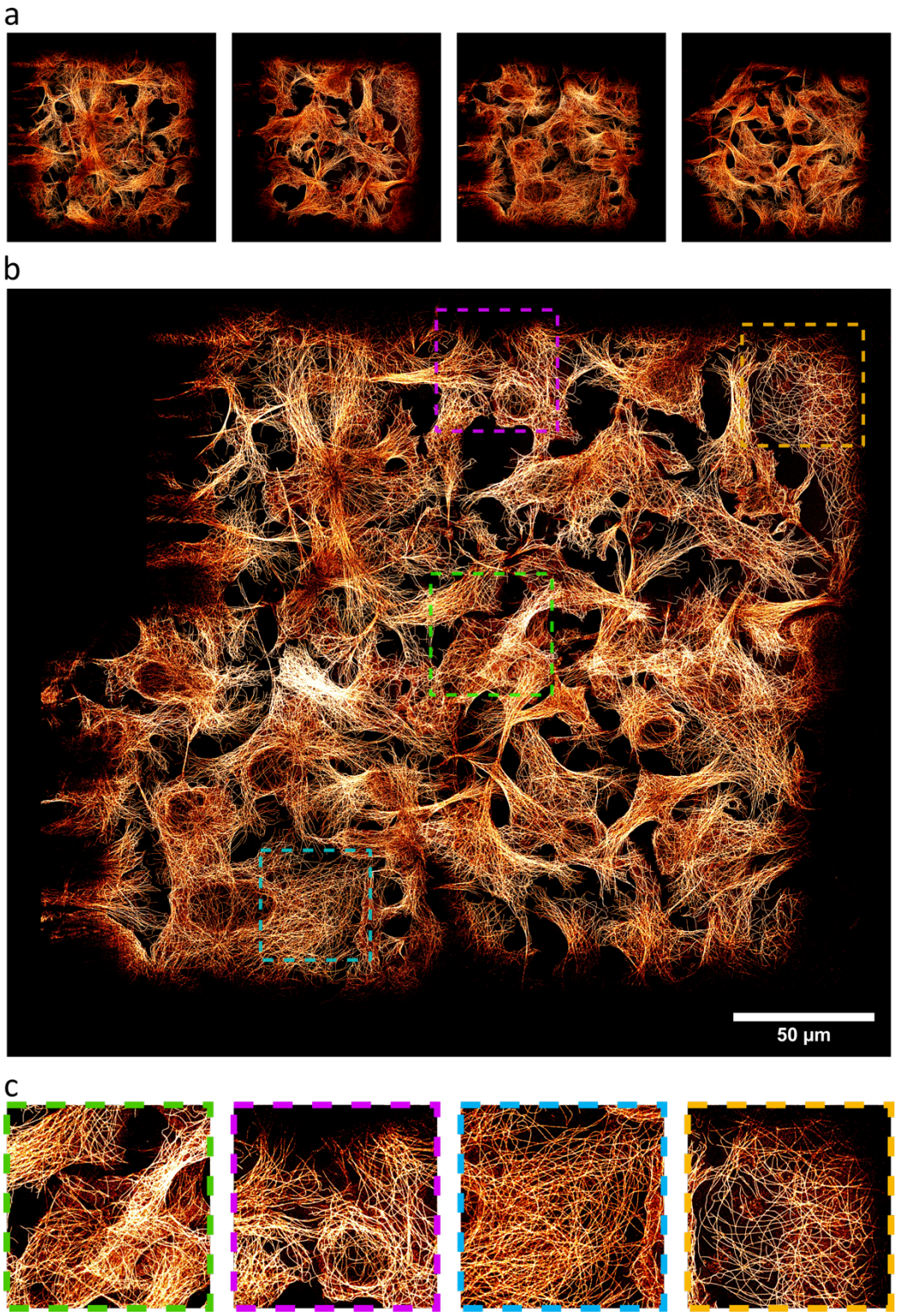

Supplementary Figure 7 Stitching of four STORM images of COS-7 labeled for microtubules, resulting in a 300 µm x 300 µm hyper-large FOV. **(a)** Individual 150 µm x 150 µm STORM images. **(b)** Stitched images resulting in a 300 µm x 300 µm field of view. (c) Close-up views of highlighted areas in (b).

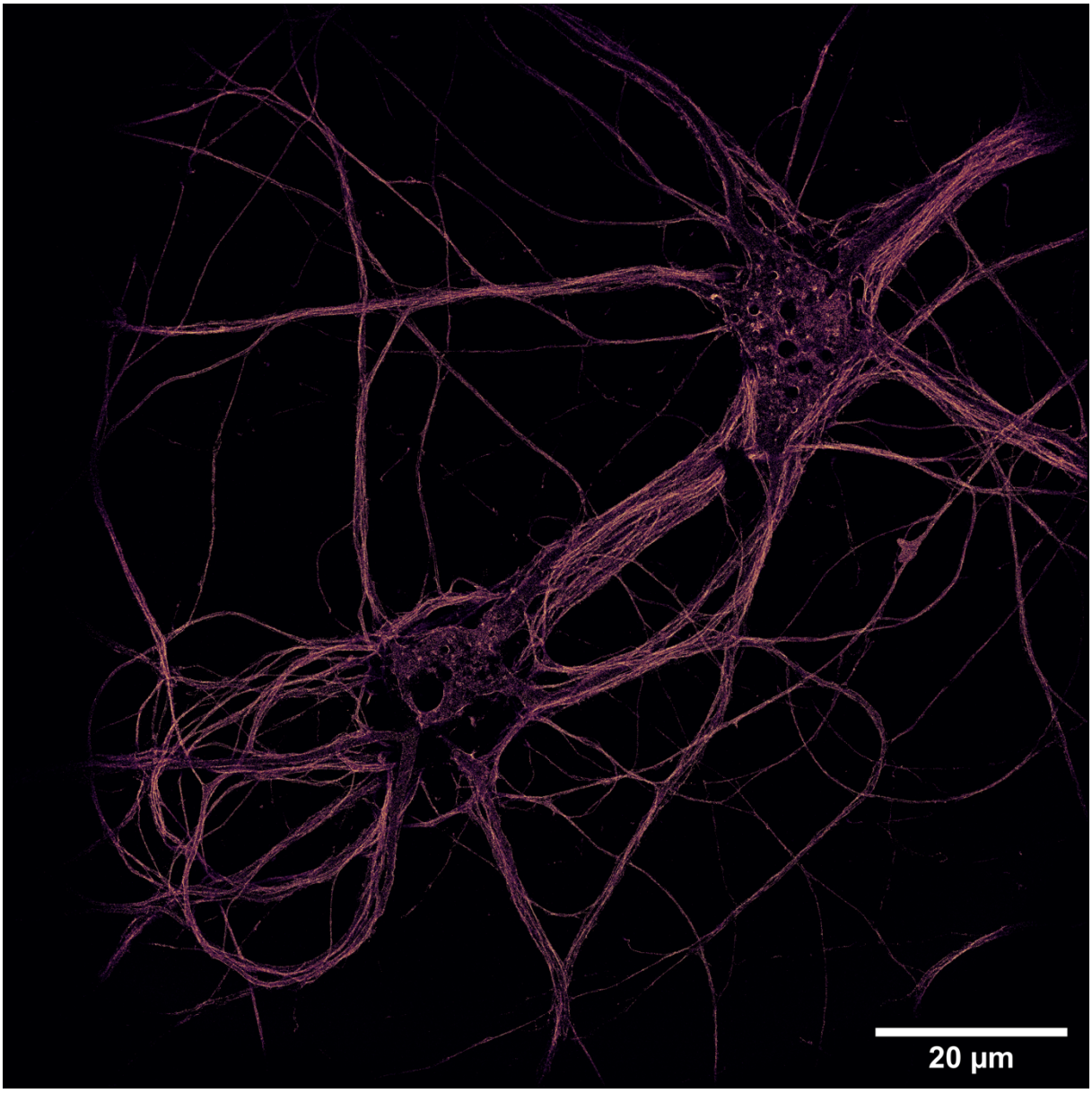

Supplementary Figure 8 STORM 120 µm x 120 µm image of neuronal β2-spectrin, labeled with AF647.